


Pr-favoured variants of the bacteriophytochrome from the plant pathogen *Xanthomonas campestris* hint on light regulation of virulence-associated mechanisms

Valeria Conforte¹, Lisandro Horacio Otero^{2,3}, Laila Toum¹, Serena Sirigu⁴, Giuliano Tomás Antelo², Jimena Rinaldi², Sabrina Foscaldi², Sebastián Klinke^{2,3}, Leonard Michel Gabriel Chavas^{4,5}, Adrián Alberto Vojnov¹, Fernando Alberto Goldbaum^{2,3}, Florencia Malamud⁶ and Hernán Ruy Bonomi² 

1 Instituto de Ciencia y Tecnología Dr. César Milstein, Fundación Pablo Cassará, Consejo Nacional de Investigaciones Científicas y Técnicas (CONICET), Ciudad Autónoma de Buenos Aires, Argentina

2 Fundación Instituto Leloir, Instituto de Investigaciones Bioquímicas de Buenos Aires (IIBBA), Consejo Nacional de Investigaciones Científicas y Técnicas (CONICET), Ciudad Autónoma de Buenos Aires, Argentina

3 Plataforma Argentina de Biología Estructural y Metabólica PLABEM, Ciudad Autónoma de Buenos Aires, Argentina

4 Synchrotron SOLEIL, L'Orme des Merisiers Saint-Aubin, Gif sur Yvette, France

5 Synchrotron Radiation Research Center, Nagoya University, Nagoya, Japan

6 Departamento de Ciencias Básicas, Universidad Nacional de Luján, Consejo Nacional de Investigaciones Científicas y Técnicas (CONICET), Luján, Buenos Aires, Argentina

Keywords

BphP; phytochrome; phytopathogen; virulence; X-ray crystallography

Correspondence

F. Malamud, Departamento de Ciencias Básicas, Universidad Nacional de Luján-CONICET, Ruta 5 y Av. Constitución (6700), Luján, Buenos Aires, Argentina

E-mail: fmalamud@iibintech.com.ar

H. R. Bonomi, Fundación Instituto Leloir-IIBBA, CONICET, Av. Patricias Argentinas 435 (C1405BWE), Ciudad Autónoma de Buenos Aires, Argentina

Tel: +054 11 5238 7500 (Extn. 2304)

E-mail: hbonomi@leloir.org.ar

Valeria Conforte and Lisandro Horacio Otero contributed equally to this work.

(Received 26 November 2020, revised 25 February 2021, accepted 14 April 2021)

doi:10.1111/febs.15883

Red/far-red light-sensing bacteriophytochrome photoreceptor (BphP) pathways play key roles in bacterial physiology and ecology. These bilin-binding proteins photoswitch between two states, Pr (red absorbing) and Pfr (far-red absorbing). The isomerization of the chromophore and the downstream structural changes result in the light signal transduction. The agricultural pathogen *Xanthomonas campestris* pv. *campestris* (*Xcc*) code for a single bathy-like type BphP (*Xcc*BphP), previously shown to negatively regulate several light-mediated biological processes involved in virulence. Here, we generated three different full-length variants with single amino acid changes within its GAF domain that affect the *Xcc*BphP photocycle favouring its Pr state: L193Q, L193N and D199A. While D199A recombinant protein locks *Xcc*BphP in a Pr-like state, L193Q and L193N exhibit a significant enrichment of the Pr form in thermal equilibrium. The X-ray crystal structures of the three variants were solved, resembling the wild-type protein in the Pr state. Finally, we studied the effects of altering the *Xcc*BphP photocycle on the exopolysaccharide xanthan production and stomatal aperture assays as readouts of its bacterial signalling pathway. Null-mutant complementation assays show that the photoactive Pr-favoured *Xcc*BphP variants L193Q and L193N tend to negatively regulate xanthan production *in vivo*. In addition, our results indicate that strains expressing these variants also promote stomatal apertures in challenged plant epidermal peels, compared to wild-type *Xcc*. The findings presented in this work provide new evidence on the Pr state of *Xcc*BphP as a negative regulator of the virulence-associated mechanisms by light in *Xcc*.

Abbreviations

BphP, bacterial phytochrome; BV, biliverdin Ix α ; EPS, exopolysaccharide; MW, molecular weight; OM, output module; Pfr, far-red-absorbing state; Pr, red-absorbing state; PSM, photosensory module; SEC, size-exclusion chromatography; SLS, static light scattering; *Xcc*, *Xanthomonas campestris* pv. *campestris*; *Xcc*BphP, bacterial phytochrome from *Xanthomonas campestris* pv. *campestris*.

Introduction

Phytochromes photoreceptors are widespread in plants and microorganisms. They are most commonly known for sensing red and far-red lights through a photosensory module (PSM) that covalently binds bilin molecules (open-chain tetrapyrroles) as chromophores to a conserved Cys residue [1]. The bilin-protein ensemble dictates their particular photochemical behaviours under certain conditions. Under red or far-red light irradiation, the bound bilin can isomerize and adopt two main photostates that differ in their spectral properties (i.e. the red-absorbing Pr and the far-red-absorbing Pfr) [2]. Based on the thermal dark ground state, phytochromes can be divided into two types: (a) canonical phytochromes, presenting a Pr ground state, and (b) bathy phytochromes, presenting a Pfr ground state [3–5].

Phytochromes were originally discovered in plants as part of red and far-red signalling networks where they are known to regulate an extended range of physiological responses including growth, development, photosynthesis and immunity [6–8]. These proteins have also been found extensively in microorganisms, such as bacteria, algae and fungi. Bacterial phytochromes, or BphPs, play key roles in bacterial physiology and in the host-microbe interaction for a wide range of organisms [9–17].

Typical BphPs share (a) biliverdin IX α (BV) as the chromophore and (b) a common structural architecture composed of an N-terminal PAS2-GAF-PHY domain triad as part of the PSM and a C-terminal variable output module (OM) [1]. OMs can be constituted by a wide range of isolated domains or combinations of them including histidine kinases, response regulators, diguanylate cyclases and phosphodiesterases, coiled-coiled/disordered/low complexity regions and PAS domains [1,18]. The OM transduces the input light signal sensed by the PSM into a biochemical or biophysical signalling output. For this to happen, a cascade of events takes place upon illumination, initiated by the isomerization of BV and followed by local rearrangement of residues near the chromophore. As a result, a protrusion from the PHY domain that interacts with the GAF domain—termed as ‘tongue’—undergoes a secondary structure refolding possibly affecting the OM positioning and, consequently, the signalling response [19–25].

Xanthomonas campestris pathovars are worldwide distributed γ -proteobacteria responsible for multiple diseases including black rot disease in cruciferous plants that impact directly on agriculture [26,27].

Xanthomonas campestris pv. *campestris* (*Xcc*) has the ability to live epiphytically and also colonize the plant xylem by entering through the stomata, hydathodes or wounds [28]. Epiphytic bacteria are exposed to nutrient limitation, fluctuating water availability, exposure to sunlight and are subjected to the diurnal light cycle and light spectrum variations. *Xcc* codes for a single BphP (*Xcc*BphP), which regulates the host-microbe interaction. We have previously reported that *Xcc*BphP exerts a regulatory effect in the *Xcc* physiology affecting its virulence factors [i.e. xanthan exopolysaccharide (EPS), extracellular hydrolytic enzymes, biofilm] and impacting in the plant defence mechanisms (i.e. callose deposition and stomatal aperture/closure) [12].

The structure and photochemistry of *Xcc*BphP has been a matter of study in recent works. It has been established that *Xcc*BphP is a bathy-like phytochrome, with Pfr as its principal component in thermal equilibrium [24]. The structure of the full-length protein in the Pr configuration has also been solved, with its complete PSM and a PAS9 domain as the OM [24,29]. This structure allowed us to generate a simple putative model for the intramolecular signalling mechanism that operates in this BphP.

The purpose of the current work was to investigate the biological role of the *Xcc*BphP photocycle. In order to study the Pr photostate in detail, we generated specific full-length site-directed mutant variants with altered photocycles (either by locking or stabilizing their Pr state), solved their structures by X-ray crystallography and interrogated the effects of altering the photocycle in bacterial physiology.

Results and Discussion

*Xcc*BphP Pr-favoured variants

Yang *et al.* [30,31] have previously shown in *Pseudomonas aeruginosa* bathy *Pa*BphP that substitutions in the GAF domain residues Gln188 and Asp194 (i.e. Q188L and D194A) favour the Pr state. The homologous positions in *Xcc*BphP are Leu193 and Asp199, respectively (Fig. 1). As *Xcc*BphP and *Pa*BphP are both bathy phytochromes, we reasoned that substitutions in these positions would lead to similar alterations in *Xcc*BphP photochemistry; thus, we designed the L193Q and D199A variants.

In a recent study, we have developed a method for screening phytochrome mutants and rapidly exploring their photochemistry in bacterial extracts. Using

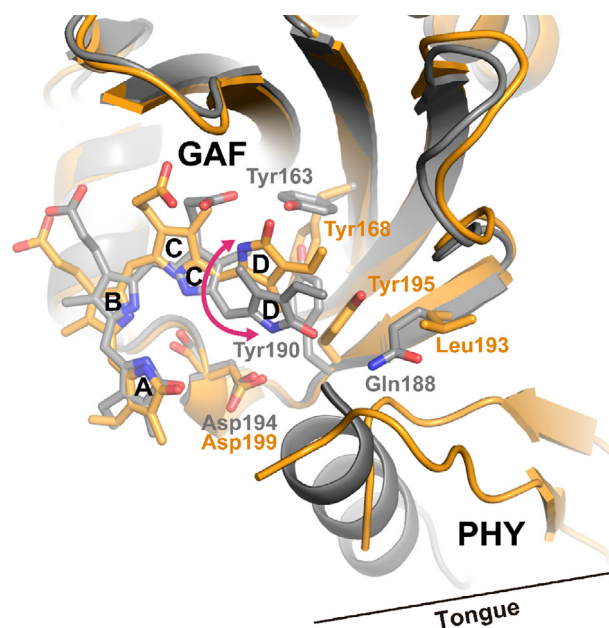


Fig. 1. *XccBphP* and *PaBphP* structural alignment. Structural alignment on the chromophore binding pocket of *XccBphP* in the Pr state (PDB code: 5AKP, orange) and *PaBphP* in the Pfr state (PDB code: 3C2W, grey) in ribbon representation. Residues Tyr168, Leu193, Tyr195 and Asp199 from *XccBphP* and residues homologues Tyr163, Gln188, Tyr190 and Asp194 from *PaBphP* are represented as sticks. The BV chromophore is represented as sticks with carbon atoms in the same colours. Oxygen and nitrogen atoms are coloured in red and blue, respectively. The four BV pyrrolic rings A, B, C and D are indicated. The reversible ring D isomerization setting the BV configurations ZZZssa (Pr state) or ZZEssa (Pfr state) is denoted by a violet arrow. The GAF and PHY domains, as well as the tongue region, are indicated for clarity. Structural representations were generated using PYMOL software version 1.8.

XccBphP as model, we included multiple Leu193 substitutions and the D199A variant [32]. Noteworthy, we have shown in this preliminary characterization that polar substitutions at Leu193 tend to favour the Pr photostate and that D199A presents a locked state reminiscent of a Pr [32].

To corroborate the bacterial extract data from the above-mentioned study and to characterize the L193Q photocycle, dark reversion experiments were performed by first irradiating pure protein samples with far-red or red light and then measuring their UV-Vis spectra as a function of time in the dark (Fig. 2A). Additionally, the Pr:Pfr composition was calculated for each time point, and then, exponential functions were fitted to the data (Fig. 2B, Eqns 1 and 2) to calculate the Pr:Pfr equilibrium composition and the half-life of the dark reversion kinetics (Table 1). As previously reported, the wild-type variant behaves as a

bathy-like phytochrome equilibrating in the dark at ~ 84% Pfr vs. ~ 16% Pr with a half-life of ~ 295 min for the Pr-to-Pfr dark reversion, showing similar values as in other works [24,32]. The L193Q substitution was found to favour the *XccBphP* Pr state, evidenced by an equilibrium Pr : Pfr ratio of ~ 2 : 1 (Fig. 2 and Table 1). If the effects of the L193Q mutation are due to the biochemical nature of the introduced amide group, then the L193N mutant should in principle have similar effects. We therefore constructed the L193N site-directed mutant and tested its photochemical properties. The behaviour of the L193N mutant is more extreme than L193Q in dark reversion experiments, presenting an enhanced stabilization of the Pr state (Fig. 2). Both L193Q and L193N exhibit very slow dark reversion rates, with half-life values greater than 1700 min Pfr-to-Pr dark reversion (Table 1). It is worth noting here that mutations L193Q and L193N induce Pr-enrichment at dark equilibria contrasting the wild-type variant, shifting them towards canonical-like types, in agreement with our previous finding for other Leu193 polar substitutions [32]. Neither mutation produces significant shifts in the wavelengths corresponding to the Pr or Pfr maxima wavelength (λ_{\max} , Table 1). As expected, the D199A mutant presents an aberrant UV-Vis absorption spectrum reminiscent of a Pr-like state, which is almost unaltered in the dark reversion assays (Fig. 2A). This is consistent with previous studies on the *Deinococcus radiodurans* bacteriophytochrome (*DrBphP*), where the D207A substitution traps the phytochrome, probably in an intermediate state, during the Pr-to-Pfr conversion [33]. Because the D199A spectra do not change, we did not perform a spectral decomposition as with the other variants. To visualize the effects of far-red and red light irradiation, the initial spectra from Fig. 2A variants are represented with their corresponding estimated Pr and Pfr components in Fig. 3.

Structural studies of L193Q, L193N and D199A

To rule out artefacts introduced by the amino acid changes, we sought to verify that the tertiary and quaternary structures of the variants remain intact. Firstly, we inferred the oligomeric state of L193Q, L193N and D199A apoproteins in solution by performing size-exclusion chromatography (SEC) coupled to static light scattering measurements (SEC-SLS). The three variants show an elution fraction that resembles the wild-type version. The molecular weight (MW) values obtained for the L193Q and L193N variants are in agreement with a dimeric arrangement (expected MW: 141 kDa), while the D199A mutant showed a slightly

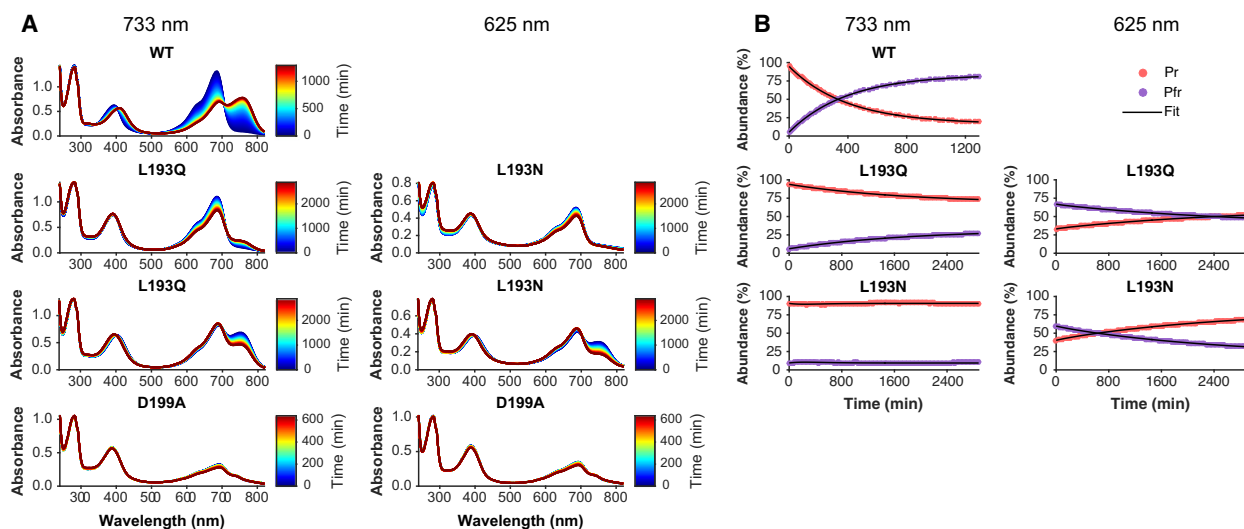


Fig. 2. UV-Vis absorption spectra of *Xcc*BphP variants. (A) Absorption spectra acquired during dark reversion of *Xcc*BphP wild-type (WT), L193Q, L193N and D199A variants after far-red (733 nm) or red initial (625 nm) illumination. Spectra from different time points are represented in colours from jet colourmap (colour bars). (B) The Pr (red) and Pfr (violet) contributions were estimated for each time point. The time courses for each variant were fitted to a double exponential function (black). Data are representative of two independent determinations.

Table 1. Kinetic parameters derived from the dark-conversion experiments from Fig. 2. Half-life was calculated using a monoexponential fit (Eqn 1), for Pr-to-Pfr and Pfr-to-Pfr conversions for bathy-like and canonical-like types, respectively. Pr and Pfr relative (%) contributions at equilibrium (Eq.) were estimated using a double exponential fit (Eqn 2). Pr and Pfr pure extrapolated spectra were used to estimate their peak wavelengths (λ_{\max}) by Gaussian fitting.

Variant	Type	Half-life (min)	Pr Eq. (%)	Pfr Eq. (%)	Pr λ_{\max} (nm)	Pfr λ_{\max} (nm)
WT	Bathy-like	295	16	84	684	758
L193Q	Canonical-like	1897	68	32	686	752
L193N	Canonical-like	1717	81	19	686	751

higher value (Fig. 4). This deviation is probably due to the interference in the scattering signal of an unidentified brownish molecule bound to the D199A apoprotein, which is not observed in the wild-type version or other mutant variants. Altogether, our results demonstrate that the quaternary dimeric arrangement in solution remains intact for the three variants.

Then, we obtained the three full-length protein structures bound to BV (Fig. 5). The structures were solved in the tetragonal space group $P4_32_12$ at 3.89 (L193Q), 3.58 (L193N) and 3.45 Å (D199A), respectively. Despite the limited diffraction resolution reached, the final refined models present good statistics with favourable stereochemistry (Table 3) and well-defined electron density. The crystal structures comprise the PSM (PAS2-GAF-PHY domains) as well as the complete OM (PAS9 domain; Fig. 5, top panel). All of them present two essentially equivalent protein chains in the asymmetric unit, which form a head-to-

head dimeric rearrangement along elongated linker helices (helical spine) in agreement with the wild-type *Xcc*BphP structure previously reported in the Pr state [24]. Accordingly, a structural comparison with the wild-type Pr state structure shows the same tertiary fold and quaternary assembly (Fig. 5, central panel), reflected in very low pairwise C^α r.m.s.d. values of 0.56 (L193Q), 0.46 (L193N) and 0.38 Å (D199A).

The BV chromophore, which is covalently linked to the Cys13 residue from the PAS2 domain and seats on the GAF domain, was found in both monomers of the three structures (Fig. 5, bottom panel). In the L193Q and L193N variants, a Pr-related *ZZZssa* chromophore configuration is clearly defined. However, in the case of D199A, the BV ring D is missing in the electron density map (Fig. 5, bottom panel) preventing an unambiguous assignment, as previously for the wild-type Pr structure [24]. The tongue region is clearly defined and adopts a β -sheet conformation (Fig. 5,

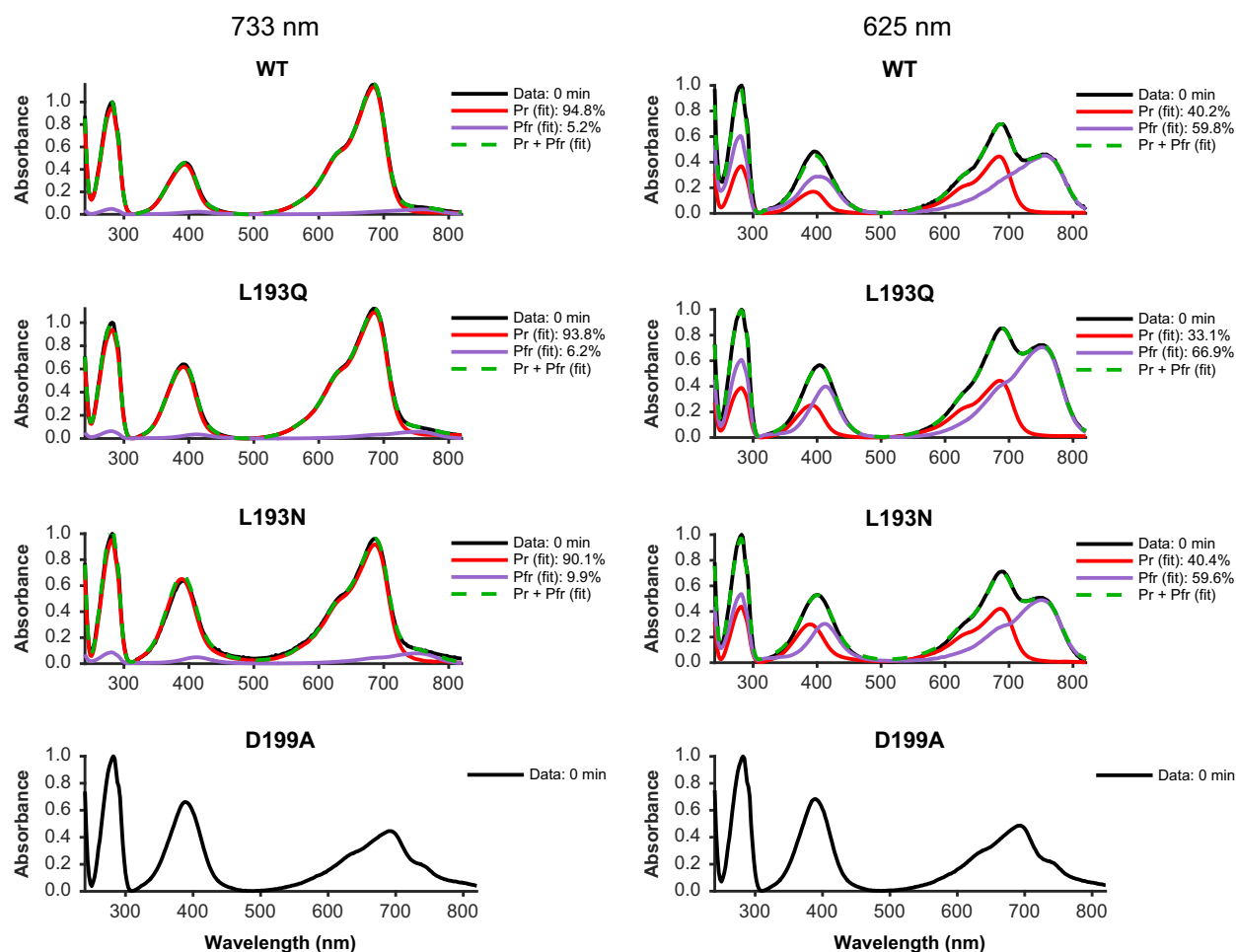


Fig. 3. UV-Vis spectra after light irradiation of *Xcc*BphP variants. The UV-Vis processed spectra after far-red (733 nm) or red irradiation (625 nm) from the series shown in Fig. 2A and from a wild-type (WT) *Xcc*BphP sample irradiated with red light are shown as black traces. Pr and Pfr relative contributions were estimated for wild-type, L193Q and L193N variants (red and purple traces, respectively). The point-to-point sums of the calculated Pr and Pfr contributions are depicted in dashed green traces. Data are representative of two independent determinations.

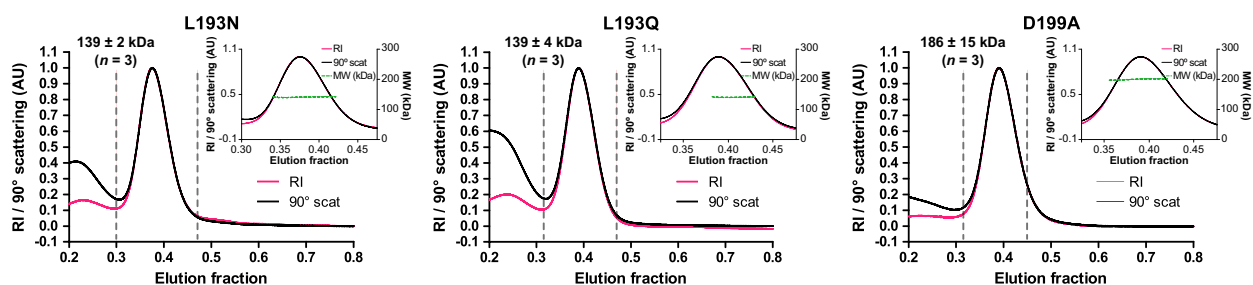


Fig. 4. SLS coupled to SEC. The apoproteins were subjected to SEC, and the average MW of the peaks was estimated from the 90° scattering and the refractive index signals. The 90° scattering and the refractive index signals are plotted versus the elution fractions. The insets show the fraction range corresponding to the peaks and the MW on the right axis. The graphs correspond to one representative experiment from each mutant variant. The MW mean \pm SD values from three independent experiments are indicated next to the peaks in each case.

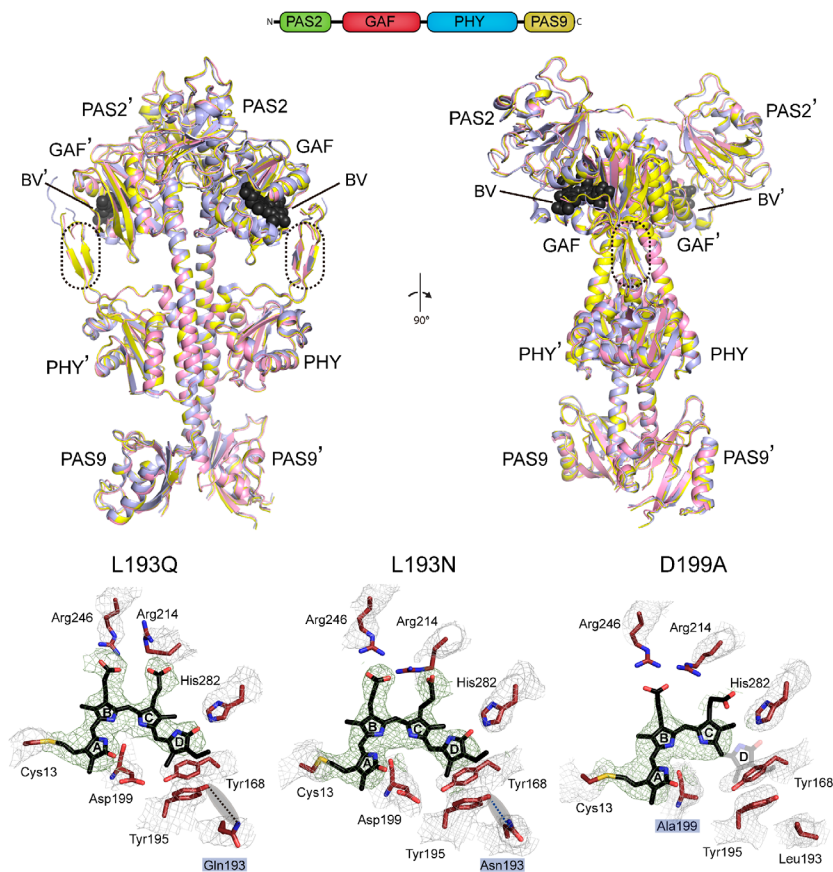


Fig. 5. Crystal structures of *Xcc*BphP variants in the Pr state. Top panel: Domain architecture of *Xcc*BphP. Central panel: Structural alignment of the overall structures of the L193Q (pink), L193N (yellow) and D199A (blue) variants with protomers A and B (indicated as prime) displayed in two different orientations rotated by 90°. The BV chromophore is represented as black spheres only in L193Q for clarity. The tongue region consisting of two β -strands is indicated with a dashed perimeter. The different domains are labelled. Bottom panel: Chromophore binding pocket of the L193Q, L193N and D199A variants. BV is shown as sticks with carbon atoms in black, oxygen atoms in red and nitrogen atoms in blue. The four BV pyrrolic rings A, B, C and D are indicated. Feature-enhanced maps [50] around the BV molecule (green mesh) and the chromophore binding pocket (grey mesh) are contoured at the 1.0 σ level. The maps were generated in Phenix [51]. In the L193Q and L193N variants, a Pr-related ZZZssa chromophore configuration is clearly defined. In D199A, the BV ring D is missing in the electron density map; therefore, its position is shown semi-transparent in the model. The most relevant residues are depicted as sticks with carbon atoms in ruby, oxygen atoms in red, nitrogen atoms in blue and sulfur atoms in yellow. The substituted residue in each structure is highlighted in a light-blue box. The potential hydrogen-bond interactions mediated by the Tyr195 hydroxyl group and the side chains of Gln193 and Asn193 are indicated by dashed lines on semi-transparent ovals coloured in grey. Molecular structures and their electron densities were represented using PYMOL version 1.8.

central panel). This observation, together with the synchronized conformations of the Tyr168 and Tyr195 residues around the BV chromophore ring D (Fig. 5, bottom panel), ratify a protein scaffold in the Pr state for the three variants. The BV global position is fairly similar in the three structures in comparison with the wild-type Pr state with no significant structural differences detected on the overall BV binding pocket.

No structural changes could be identified around the residue position 193 in the variants L193Q and L193N with respect to the wild-type Pr structure (data not shown). One possible scenario explaining the relative

stabilizing of the Pr state is that the Leu193 aliphatic side chain may be located in a hydrophobic pocket in Pfr state. The substitution of this residue with polar ones may cause a destabilization of that state favouring the Pr with varying degrees dictated by their side-chain hydrophobicity. Another possibility would involve a new hydrogen-bond between the polar side chains of Asn or Gln with the OH group from Tyr195 at the Pr position (Fig. 5, bottom panel).

As previously reported in other BphP structures in Pr, the Asp residue from the DIP motif in the GAF domain (Asp199 in *Xcc*BphP) interacts through a salt-

bridge with the Arg residue from the PRxSF motif in PHY-tongue domain (Arg472 in *Xcc*BphP). Thus, this interaction has been proposed to be necessary for the stabilization of the tongue β -sheet arrangement [18,34]. As defined in the *Xcc*BphP Pr structures from the wild-type and the variants here presented, the tongue region where the Arg residue is placed is highly unstable and the consequent salt-bridge interaction is not always defined in the electron density map. Although the presence of the β -sheet arrangement of the tongue is defined in the Pr structures from wild-type [24] and D199A (Fig. 5, central panel), and thus the salt-bridge interaction does not seem to be crucial for this particular tongue structural conformation, further structural evidences must be provided to support the role of the Asp199/Arg472 salt-bridge in the Pr state.

In agreement, the crystal structure of the homolog substitution D207A from *D. radiodurans* phytochrome *Dr*BphP (PAS-GAF construct) [35] showed an almost identical folding in the chromophore binding domain in comparison with the wild-type solved in the Pr state [36]. Among the minor differences appreciated, a slight rotation on the Tyr263 (Tyr255 in *Xcc*BphP) from the α -helix closing the chromophore binding pocket on the top is observed. This subtle change in *Dr*BphP-D207A has been proposed to be as a consequence of the abolished interaction between the tyrosine hydroxyl group and the carboxylate moiety from the DIP motif aspartic in the Pr state [35], which appears to play a central role in mediating the photochemical process of phytochromes [36]. Although the Asp199 carboxylate was also found interacting with the Tyr255 in the Pr state of wild-type *Xcc*BphP [24], and therefore, this slight tyrosine rotation aforementioned may be occurring in D199A, and this is not appreciated in the crystal structure reported here due to low resolution reached.

Altogether, our results show that the Pr state from L193Q, L193N and D199A crystal structures display no major changes compared to wild-type Pr structure. However, their differential photochemical behaviours may be explained by alterations in the intermediate states (i.e. Lumi and Meta) or minor changes not detected at these structural resolutions, (e.g. side-chain modifications, water molecules positions) [34].

The Pr state acts as a negative regulator in *Xcc*

In a previous work, we have demonstrated that light regulates xanthan production in *Xcc* [12]. We have shown that wild-type *Xcc* produces more EPS in dark conditions than in white light and that the *Xccbphp* null mutant is insensitive to light producing more xanthan in both conditions. Hence, here we use EPS

production as a proxy of *Xcc*BphP signalling activity. To better understand the role of the Pr:Pfr photocycle in the bacterial physiology and to evaluate whether Pr-favoured variants are able to signal and modulate xanthan production *in vivo*, we proceeded to complement the *Xccbphp* null mutant with overexpressing plasmids coding for the L193Q, L193N and D199A protein variants (strains pL193Q, pL193N and pD199A, respectively) and a control strain bearing a wild-type copy of the *Xccbphp* (p*Xcc*BphP). The bacterial strains were cultured under red light, far-red light or in dark conditions and extracellular EPS was subsequently quantified. As expected from previous results [12], the *Xccbphp* mutant is insensitive to the light treatment. We observed that the EPS production in the *Xccbphp* mutant is higher than in the wild-type strain *Xcc* in all conditions assayed. The complemented control p*Xcc*BphP presented a behaviour similar to the wild-type strain, but with more pronounced responses to the treatments, particularly with far-red light (Fig. 6). The latter can be associated with differential protein expression, as the complemented strain exhibits overexpression (Fig. 7), and a possible amplification of the signalling by the *Xcc*BphP pathway. Interestingly, the amounts of EPS quantified in the pL193Q and

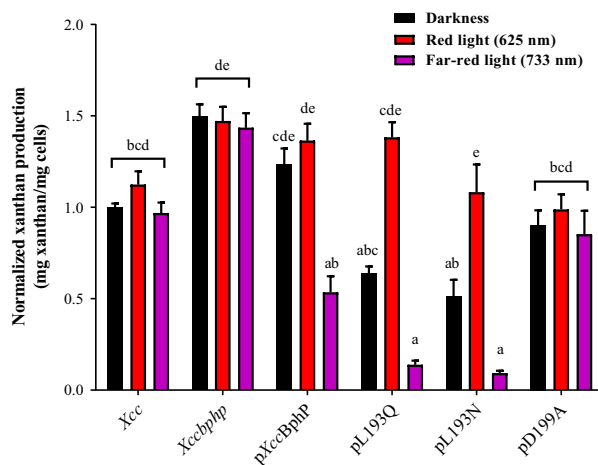


Fig. 6. Xanthan production under different lighting conditions during growth. Wild-type (*Xcc*), *Xccbphp*, p*Xccbphp*, pL193Q, pL193N and pD199A were grown in 20 mL PYM media supplemented with 2% glucose under dark, red light (625 nm) or far-red (733 nm) light conditions. Xanthan was purified through ethanol precipitation of cell-free supernatants. Cells pellets and precipitated extracellular xanthan were dried and weighed. Data are represented by mean values \pm SEM from five independent experiments (three replicates per experiment). Data were analysed using two way ANOVA followed by Tukey's post-test. Different letters indicate significant differences between groups ($P < 0.05$).

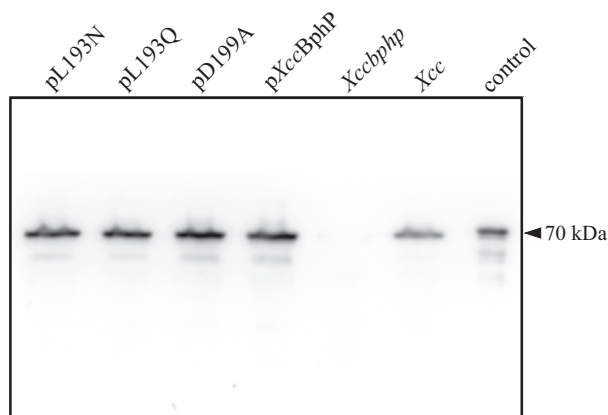


Fig. 7. Detection of *XccBphP* proteins in *Xcc* strains. Western blot of pL193N, pL193Q, pD199A, p*XccBphP*, *Xccbphp* and wild-type (*Xcc*) strains using a primary mouse polyclonal antibody anti-*XccBphP*, a secondary goat anti-mouse IgG (Fc specific) coupled to peroxidase and chemiluminescent substrate. Purified wild-type *XccBphP* protein was used as control.

pL193N complemented strains were significantly lower compared to the wild-type, p*XccBphP* and *Xccbphp* strains in dark condition. When the strains were cultured under red light, it was observed that p*XccBphP*, pL193Q and pL193N produced significantly more EPS than in darkness. In contrast, when these strains were cultured under far-red light, their EPS production was diminished (Fig. 6). Xanthan production is also reduced in the pD199A complemented strain when compared to the *Xccbphp* mutant in all conditions assayed. In addition, the pD199A complemented strain produced equivalent amounts of xanthan in all light treatments.

These results indicate that D199A is not photoactive *in vivo*, recapitulating the *in vitro* results from Fig. 2. Additionally, they suggest that L193Q and L193N do have the ability to photoswitch between Pr and Pfr *in vivo*, where the regulation of the EPS biosynthetic pathway changes with the lighting growth conditions for the complemented strains. The differences found *in vivo* can be paralleled with what is observed *in vitro* where the pL193N strain, expressing the most Pr-favoured variants, presents the lowest EPS production in the complementation assay in Pr promoting conditions (under far-red light or darkness). Taken together, these results point towards Pr being the form that negatively regulates xanthan production *in vivo* in *Xcc*.

Stomata are microscopic pores present at the aerial part of terrestrial plants, which allow them to control gas exchange and water loss. *Xcc*, like other plant pathogens, is able to regulate the opening and closure of these pores [28]. In a previous work, we have

observed that the *Xccbphp* mutant presents a deregulation of these mechanisms and is heightened in maintaining plant stomata open, where stomata from epidermal peels incubated with the *Xccbphp* mutant remained significantly opened at 1 h postincubation (h.p.i.) compared with wild-type *Xcc* [12].

In order to answer whether altering the Pr:Pfr enrichment modifies the *Xcc* ability to penetrate into the host through stomata, we performed an stomatal assay in which epidermal peels were incubated in the presence of the different bacterial strains grown in the dark. As expected from our previous results [12], stomata incubated with wild-type *Xcc* or p*XccBphP* remained significantly closed at 1 h.p.i. in a similar manner (Fig. 8). Incubation with the complemented pL193Q or pL193N strains scarcely prevented stomatal closure compared to the wild-type, although only pL193N presented statistical differences. The strain pD199A was also found to be in the same statistical group as the wild-type and p*XccBphP* strains, showing no significant differences among them. By favouring the Pr state *in vivo*, through the overexpression of the L193N variant, results in an increased stomatal aperture compared to expressing *XccBphP* wild-type. Although this phenotype is not as pronounced as in the *Xccbphp* mutant, the L193Q mutant did not show

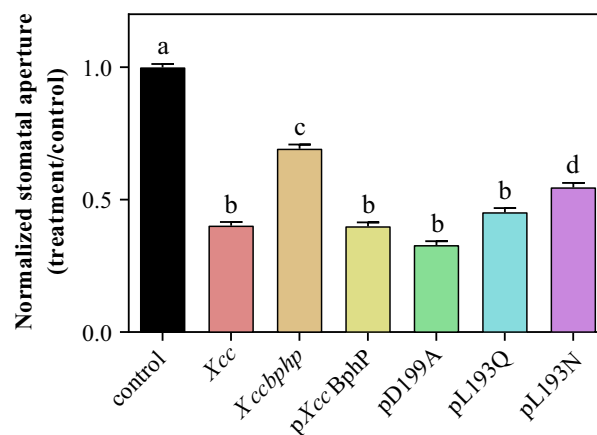


Fig. 8. Stomatal apertures in the presence of the different bacterial strains. *Arabidopsis thaliana* epidermis were incubated with a suspension of 10^8 CFU·mL⁻¹ of wild-type (*Xcc*), *Xccbphp*, p*XccBphP*, pL193Q, pL193N or pD199A bacterial strains grown in the dark. After 1 h of incubation, stomatal apertures were measured. Control: incubation in a buffer without bacteria. Values are expressed as mean \pm SEM from four independent experiments (40 replicates per experiment). Statistical significance was calculated by applying the nonparametric Kruskal–Wallis test. Different letters indicate significant differences between groups ($P < 0.05$).

this pattern, indicating differences among the effects of the amino acid substitutions.

One possible ecological scenario lies in that *Xcc* can position outside the leaves in the darkness or under canopy-filtered sunlight enriched in far-red wavelengths, with a *Xcc*BphP Pr:Pfr ratio shifted towards the Pr state, which consequently lowers xanthan production and stimulates stomata to remain open. This would favour bacterial invasion by bypassing this plant defence and pivoting *Xcc* towards a lower biofilm-producing mode, hence presenting more mobility. This vision is in agreement with Beattie *et al.* [37], where they propose that bacteria inside the plant and exposed to a varying degree of red and far-red wavelengths caused by sunlight filtered through plant tissues, tweak their mobility/biofilm modes helping them navigate the vascular system and colonizing the rest of the plant. Also in agreement with this proposition, our previous findings show in *Xcc* regulation of flagellar and xanthan genes at the transcriptional level by *Xcc*BphP, and where flagellar genes were up-regulated upon far-red light irradiation [12].

Moreover, a recent report by Verma *et al.* [17] indicates that in *Xanthomonas oryzae* pv. *oryzae* (*Xoo*), the light transduction pathway of its bacteriophytochrome (*Xoo*BphP) regulates EPS production and biofilm formation (among other processes) and that the bacterial second messenger c-di-GMP plays a role in that regulation. It has also been established that c-di-GMP intracellular levels, modulated by GGDEF and EAL protein domains, regulate the above-mentioned processes in *Xcc* [27,38]. This bacterium codes for several proteins bearing these domains, many of which also include PAS domains and other protein-protein interaction modules, which could potentially participate in the *Xcc*BphP downstream signalling pathway.

Our study indicates that sunlight could influence the host-microbe interaction in *Xcc* through the Pr state of *Xcc*BphP, which acts as a negative regulator for key and well established virulence-associated mechanisms.

Materials and methods

Bacterial strains and culture conditions

Xanthomonas campestris pv. *campestris* 8004 (*Xcc*) strains were cultured in PYM [39] at 28 °C with agitation (250 r.p.m.). *Escherichia coli* strains were cultured at 37 °C in Luria-Bertani medium with agitation (250 r.p.m.). When required, 50 µg·mL⁻¹ rifampicin (Rif), 50 µg·mL⁻¹ kanamycin, 100 µg·mL⁻¹ spectinomycin, 20 µg·mL⁻¹ chloramphenicol and 100 µg·mL⁻¹ ampicillin were added in final antibiotic concentrations. Bacteria were grown under red

(625 nm) or far-red (733 nm) continuous light at approximately 0.2 and 0.6 µmol·m⁻²·s⁻¹, respectively, from LED sources, or in darkness by covering the plates or flasks with double aluminium foil. All strains presented similar growth curves under the different light treatments (Fig. 9).

Generation of the *Xcc* bacterial strains

The *Xccbphp* mutant and *Xccbphp* complemented strains are derived from a previous work [12]. Briefly, the *Xccbphp* gene (XC_4241) was partially deleted and replaced by a 2 kb Smr/Spcr cassette (Ω) using two fragments from the flanking regions of *Xccbphp*. Complementation of *Xccbphp* was achieved by cloning a 2.7-kb fragment containing the complete XC_4242-XC_4241 operon and its regulatory sequences into the pBBR1MCS2 vector (yielding the pBBR-*Xcc*BphP vector), which was used to transform *Xccbphp* to generate the p*Xcc*BphP strain. The site-directed mutant complemented strains were generated first by constructing the mutant versions of the pBBR-*Xcc*BphP template. Briefly, this was achieved by whole plasmid amplification using Q5 High-Fidelity DNA Polymerase (New England Biolabs, Ipswich, MA, USA), the corresponding set specific primers (Table 2) and finally digesting the template from the reaction mix with the DpnI restriction enzyme (New England Biolabs), in all steps following the manufacturer's instructions. Clones were isolated and sequenced. Then, the resulting positive mutant vectors were used to transform *Xccbphp*.

Western blot

Bacterial extracts normalized by optical density at 600 nm (OD₆₀₀) were loaded and separated by SDS/PAGE (12.5% gel). Similar amounts of total protein were loaded into each lane. Proteins were transferred to Immobilon-P PVDF membranes (Millipore, Billerica, MA, USA). Membranes were blocked with nonfat milk in Tris-Buffered Saline, 0.05% Tween-20 and incubated with an anti-*Xcc*BphP polyclonal antibody (1 : 500) and then with anti-mouse IgG (Fc specific)-peroxidase antibody produced in goat (Sigma-Aldrich, St. Louis, MO, USA; 1 : 5000). Detection was achieved using the SuperSignal West Pico Chemiluminescent Substrate (Life Technologies Corporation, Carlsbad, CA, USA) on a Syngene G:BOX Chemi XRQ apparatus (Syngene, Cambridge, UK) (Fig. 7).

Generation and purification of *Xcc*BphP recombinant proteins

The pET-24a-*Xcc*BphP expression vector coding for the wild-type version of the *Xcc*BphP protein was generated in previous works [24,29] and was used as a template for site-directed mutagenesis by whole plasmid amplification using

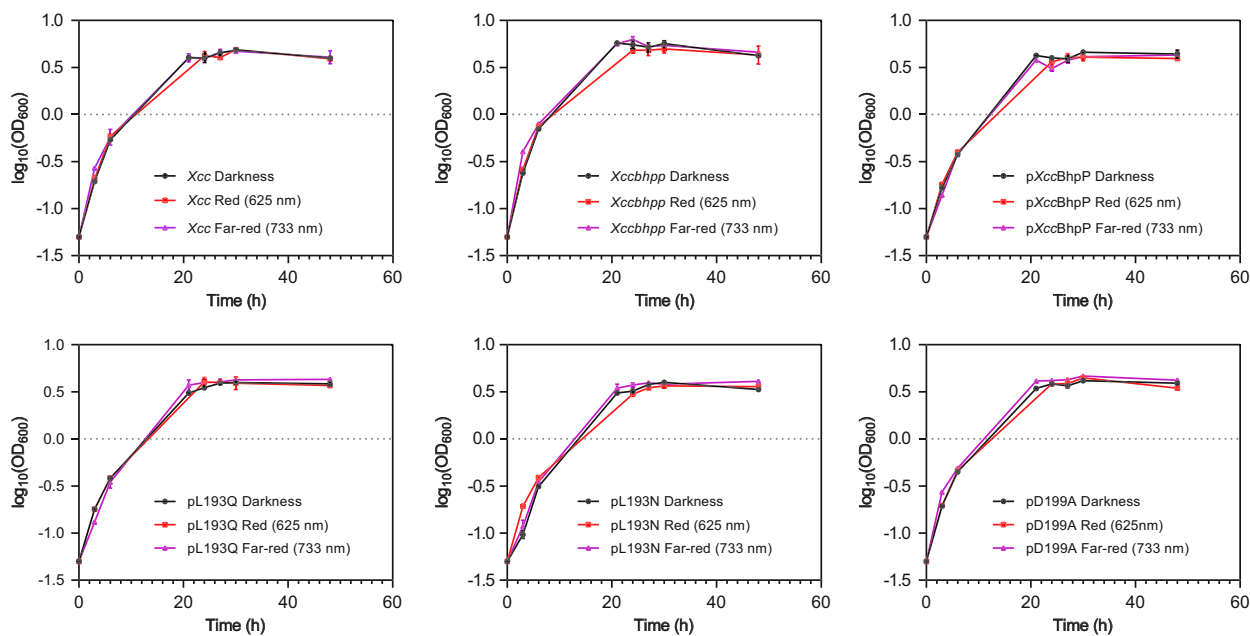


Fig. 9. Growth curves for *Xcc* strains under different light treatments. Wild-type (*Xcc*), *Xccbphp*, *pXccBhpP*, *pL193Q*, *pL193N* and *pD199A* strains were cultured in PYM media for 48 h in darkness or under red (625 nm) or far-red (733 nm) lights and their OD_{600} values were recorded at different time points. Values are expressed as mean \pm SD ($n = 3$ replicates). Data represent one of two independent determinations.

Q5 High-Fidelity DNA Polymerase, the corresponding set specific primers (Table 2) and finally digesting the methylated template from the reaction mix with DpnI (New England Biolabs, Ipswich, MA, USA), following the manufacturers' instructions. Clones were isolated and sequenced. Positive mutant vectors were used to transform *E. coli BL21(DE3)pLysE* for recombinant protein production.

Bacterial strains harbouring each expression vector were cultured and induced with a final concentration of 0.4 mM IPTG overnight at 20 °C with agitation (250 r.p.m.). Cells were harvested, ruptured by sonication and then ultracentrifuged. Proteins were purified as previously described [29]. Briefly, the supernatants were filtered and the His-tagged apoproteins purified using a His-Trap HP column (all columns from GE Healthcare Life Sciences, Piscataway, NJ, USA). Holoproteins were produced by incubation of the apoproteins for 1 h at room temperature with three-fold molar excess of BV (Sigma-Aldrich, St. Louis, MO, USA) and then subjected to SEC on a Superdex 200 16/60 column. Protein concentrations were estimated using the calculated molar extinction coefficient ϵ at 280 nm provided by the ExPASy ProtParam tool (<https://web.expasy.org/protparam/>) based on the polypeptide sequences.

UV-Vis spectroscopy and data analyses

Dark-conversion experiments were initiated in quartz cuvettes containing holoprotein solutions of *XccBhpP* or its

variants at $\sim 1 \text{ mg}\cdot\text{mL}^{-1}$ in 50 mM Tris-HCl, 250 mM NaCl, pH 7.5, at 25 °C. Samples were irradiated for 20 min with red (630 nm) 1-W LED light or for 7 min with far-red (733 nm) 0.7-W LED light. Sequential absorption spectra were recorded in dark conditions in a UV-Vis spectrophotometer (Model Cary 60; Agilent Technologies, Santa Clara, CA, USA) with an installed temperature control Peltier module.

The pure-Pr and pure-Pfr spectral shapes were calculated using data derived from the dark-conversion datasets initially illuminated with far-red and/or red light. The spectra most enriched in Pr (highest $\text{Abs}_{684 \text{ nm}} : \text{Abs}_{754 \text{ nm}}$ ratio) or Pfr (lowest $\text{Abs}_{684 \text{ nm}} : \text{Abs}_{754 \text{ nm}}$ ratio) in the variant datasets were selected (Pr-enriched and Pfr-enriched, respectively). The pure-Pfr was calculated similarly as previously described by Assafa *et al.* [40]. Briefly, a series of spectra was generated by subtracting the Pfr-enriched spectrum with increment fractions (0–1 with increment steps of 0.001) of the Pr-enriched spectrum. The derivative spectra of the subtraction series were subsequently calculated, and the minima and maxima around the wavelength corresponding to the Pfr maximum were determined. Finally, the pure-Pfr was estimated as the subtraction that minimized the difference of the derivatives corresponding to the above-mentioned minima and the maxima wavelengths (Fig. 10A).

The pure-Pr was estimated, first, by calculating a series of spectra subtracting the Pr-enriched spectrum with increment fractions (0–1 with increment steps of 0.001) of the

Table 2. Primers, plasmids and strains used in this study.

Primer	Sequence (5'–3')	Source
D199A_F	gcctatctcggcctgcattacccccgccagcgcgatccccggcgcagggcgcgcgcgctgtacctg	This work
D199A_R	caggtacagcgcgcgcgcctgcgccgggatcgcgctggcgggtaatgcaggccgagataggc	This work
L193Q_F	cgcaagccggagctggaggcctatctcggccagcattacccccgccagcgcacatccccggcgcag	This work
L193Q_R	ctgcgccgggatgtcgctggcgggtaatgctggccgagataggcctccagctccggcttgcg	This work
L193N_F	cgcaagccggagctggaggcctatctcggcaaccattacccccgccagcgcacatccccggcgcag	This work
L193N_R	ctgcgccgggatgtcgctggcgggtaatggttgccgagataggcctccagctccggcttgcg	This work
Plasmid	Parental template/primers used/characteristics	Source
pET-24a- <i>XccBphP</i>	Full-length Hisx6- <i>XccBphP</i> (residues 1–634) cloned from XC_4241 ORF	[24,29]
pET-24a- <i>XccBphP</i> -D199A	pET-24a- <i>XccBphP</i> /D199A_F-D199A_R	This work
pET-24a- <i>XccBphP</i> -L193Q	pET-24a- <i>XccBphP</i> /L193Q_F-L193Q_R	This work
pET-24a- <i>XccBphP</i> -L193N	pET-24a- <i>XccBphP</i> /L193N_F-L193N_R	This work
pBBR- <i>XccBphP</i>	pBBR1-MCS2 with a 2,708-bp fragment containing <i>XccbphO-XccbphP</i> operon and 5' regulatory sequence	[12]
pBBR- <i>XccBphP</i> -D199A	pBBR- <i>XccBphP</i> /D199A_F-D199A_R	This work
pBBR- <i>XccBphP</i> -L193Q	pBBR- <i>XccBphP</i> /L193Q_F-L193Q_R	This work
pBBR- <i>XccBphP</i> -L193N	pBBR- <i>XccBphP</i> /L193N_F-L193N_R	This work
Strain	Genotype/relevant characteristics	Source
<i>Xcc</i>	<i>Xanthomonas campestris</i> pv. <i>campestris</i> 8004, Rif ^r	Laboratory stock
DE3- <i>XccBphP</i>	<i>Escherichia coli</i> BL21(DE3)pLysE + pET-24a- <i>XccBphP</i> , Cm ^r , Km ^r	[24,29]
DE3-D199A	<i>Escherichia coli</i> BL21(DE3)pLysE + pET-24a- <i>XccBphP</i> -D199A, Cm ^r , Km ^r	This work
DE3-L193Q	<i>Escherichia coli</i> BL21(DE3)pLysE + pET-24a- <i>XccBphP</i> -L193Q, Cm ^r , Km ^r	This work
DE3-L193N	<i>Escherichia coli</i> BL21(DE3)pLysE + pET-24a- <i>XccBphP</i> -L193N, Cm ^r , Km ^r	This work
<i>XccbphP</i>	<i>Xcc</i> , XC_4241::Ω, Rif ^r , Spc ^r	[12]
p <i>XccbphP</i>	<i>XccbphP</i> + pBBR- <i>XccBphP</i> , Rif ^r , Spc ^r , Km ^r	[12]
pD199A	<i>XccbphP</i> + pBBR-D199A, Rif ^r , Spc ^r , Km ^r	This work
pL193Q	<i>XccbphP</i> + pBBR-L193Q, Rif ^r , Spc ^r , Km ^r	This work
pL193N	<i>XccbphP</i> + pBBR-L193N, Rif ^r , Spc ^r , Km ^r	This work

pure-Pr spectrum. Then, the derivative spectra of the subtractions were subsequently calculated, and for each one of them, a mean and standard deviation (SD) were calculated in the range between the wavelength corresponding to the Pr maxima and the highest wavelength in the data set (820 nm). Finally, the pure-Pr spectrum was calculated by the subtraction of the pure-Pr fraction corresponding to the local maxima produced by the multiplication of the mean and SD values of the derivative spectra in the selected range (Fig. 10B).

Then, each spectrum was assumed to be composed of two pure components, and the linear combinations of their pure-Pr and pure-Pfr spectra were calculated to best fit the data set using data corresponding to wavelengths above 510 nm. This allowed to obtain the individual Pr and Pfr spectra at each time point that, added together, reconstituted the experimental dataset. The Pr and Pfr abundances

(%) at each time were estimated as the relative spectral area corresponding to the pure-Pr and the pure-Pfr with respect to the sum of the areas (using the data corresponding to wavelengths above 510 nm).

The kinetic analysis was carried out by optimizing the parameters of a double exponential model (Eq. 1) and a monoexponential model (Eq. 2) to fit the Pr/Pfr abundance data. The Pr or Pfr equilibrium values were derived from the parameter A of the double exponential fitting, while the monoexponential model was used to estimate half-life values using the parameter H (Table 1).

$$f(t) = A + B \cdot e^{-t/\tau} + D \cdot e^{-t/\tau'} \quad (1)$$

$$f(t) = F + G \cdot e^{-t/H} \quad (2)$$

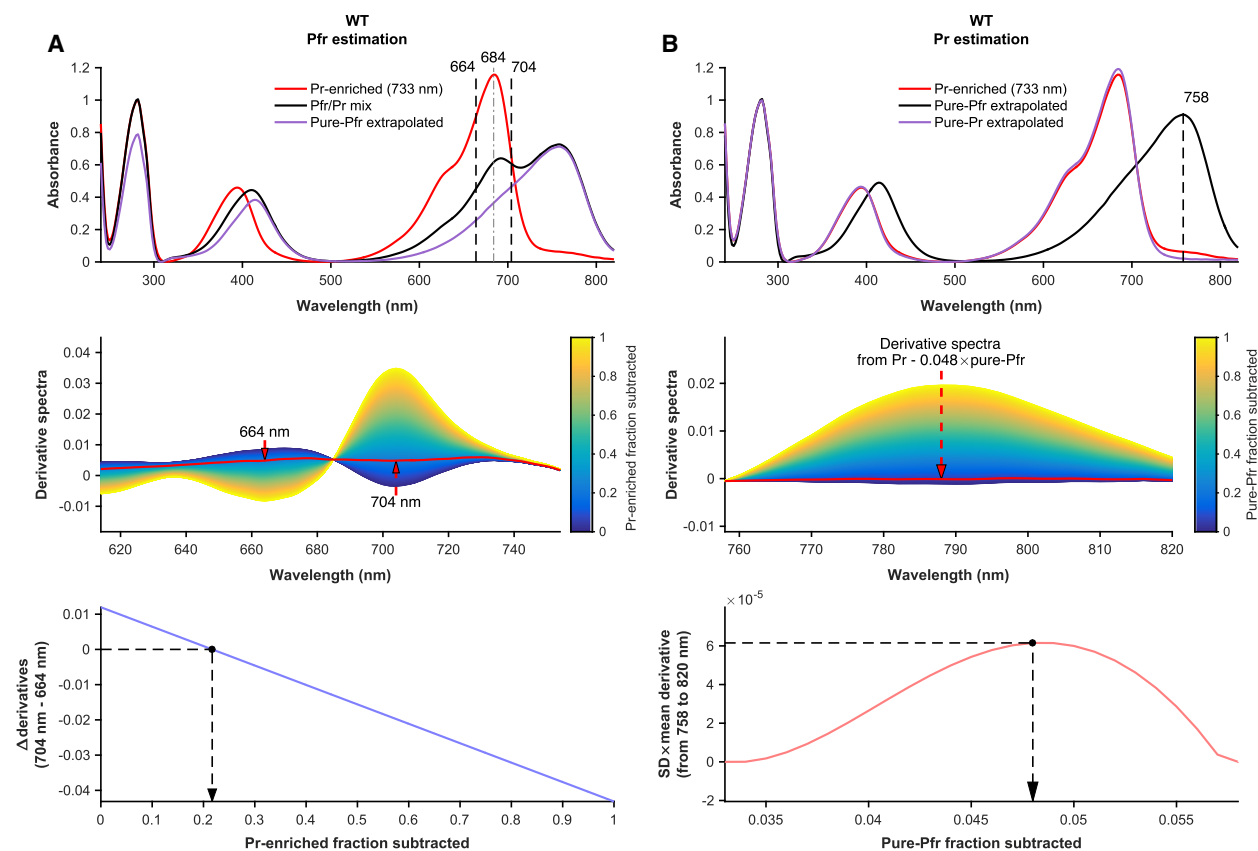


Fig. 10. Extrapolation of pure-Pr and pure-Pfr spectral components. The pure-Pr and pure-Pfr spectra were calculated using data derived from the dark-conversion datasets initially illuminated with far-red light and/or red light (top panels, Pr-enriched and Pfr/Pr mix spectra). (A) Pure-Pfr estimation. A series of derivative spectra were generated after subtracting the Pfr-enriched spectrum with increment fractions of the Pr-enriched spectrum (middle panel). The minima and maxima around the wavelength corresponding to the Pfr maximum were determined (red arrows). The pure-Pfr spectrum shape was estimated as the subtraction which minimized the difference of the derivatives corresponding to the above-mentioned minima and the maxima wavelengths (bottom panel, the Pr-enriched fraction selected for the subtraction is indicated with a black dashed arrow). (B) Pure-Pr estimation. A series of derivative spectra were generated after subtracting the Pr-enriched spectrum with increment fractions of the pure-Pfr spectrum (middle panel). The mean and standard deviation (SD) were calculated for each derivative spectrum in the range between the wavelength corresponding to the Pfr maxima and the highest wavelength in the data set (820 nm). The pure-Pr spectrum shape was calculated by the subtraction of the pure-Pfr fraction corresponding to the local maxima produced by the multiplication of the mean and SD values of the derivative spectra in the selected range (bottom panel, the pure-Pfr fraction selected for the subtraction is indicated with a black dashed arrow). Panels A and B show as example the pure-Pr and pure-Pfr extrapolations for the *XccBphP* wild-type variant. These procedures were performed to all variants in this study.

As an example, a processed data set for the wild-type version is available in GIF format (WT_Far-red.gif) as [Supplementary Information](#), overlaying individual pure-Pr and Pfr spectral components, and their relative abundances at each time point. All steps of the analysis were performed using custom made scripts developed in MATLAB software (version 2015b, Mathworks, Inc., Natick, MA, USA; scripts available if requested).

SEC-SLS measurements

The average MWs and oligomeric state of *XccBphP* and its variants were determined (Fig. 4) using a PD2010 90° light scattering instrument (Precision Detectors, Bellingham,

MA, USA) connected in tandem to a high-performance liquid chromatography system and an LKB 2142 Differential Refractometer Detector (Pharmacia, Uppsala, Sweden). Only MWs for apoproteins could be calculated due to the interference produced by BV in the 90° light scattering measurements because of its absorption in the laser wavelength (685 nm, AlGaInP). A Superdex 200 HR-10/30 column (24 mL) was used with isocratic elution in 50 mM Tris-HCl, 250 mM NaCl, pH 7.7, at a flow rate of 0.4 mL·min⁻¹ at 20 °C, with 0.65–0.10 mg of injected protein sample. The MW was calculated relating its 90° to the IR signals using the software Discovery32 supplied by Precision Detectors. Bovine serum albumin (MW 66.5 kDa) was used as a standard.

Table 3. Crystallographic table.

	L193Q	L193N	D199A
Data collection			
Beamline	PROXIMA-1	PROXIMA-1	PROXIMA-2A
Detector	PILATUS 6 M	PILATUS 6 M	EIGER X 9 M
Number of frames	2850	3600	1800
Oscillation step (deg)	0.1	0.1	0.1
Wavelength (Å)	0.97857	0.97857	0.9801
Exposure per frame (s)	0.1	0.1	0.025
Indexing and scaling			
Cell parameters			
$a = b$ (Å)	103.22	103.60	103.86
c (Å)	344.20	343.69	342.61
$\alpha = \beta = \gamma$ (deg)	90	90	90
Space group	$P4_32_12$	$P4_32_12$	$P4_32_12$
Resolution limit (Å)	3.89	3.58	3.45
No. of total reflections	358 080	579 247	319 572
No. of unique reflections	17 904	22 805	25 772
Average multiplicity ^a	20.0 (19.0)	25.4 (24.8)	12.4 (12.0)
$\langle I/\sigma(I) \rangle$	8.5 (1.1)	13.2 (1.4)	10.6 (1.7)
R_{merge}	0.301 (3.351)	0.211 (2.892)	0.165 (1.536)
R_{pim}	0.053 (0.586)	0.043 (0.599)	0.048 (0.459)
R_{sym}	0.327 (3.116)	0.200 (2.421)	0.172 (1.605)
CC1/2 (%)	99.7 (43.1)	99.9 (46.2)	99.0 (69.0)
Completeness (%)	99.6 (97.4)	99.3 (93.5)	100.0 (100.0)
No. of chains per asymmetric unit	2	2	2
Solvent content (%)	62	62	62
Overall B -factor (Wilson plot, Å ²)	151	116	124
Refinement			
Resolution range (Å)	49.43 – 3.89	49.60 – 3.58	47.27 – 3.45
Number of protein atoms	9321	9374	9367
Number of ligand atoms	86	86	86
Number of water molecules	-	2	2
R	0.216	0.198	0.23
R_{free}	0.27	0.238	0.25
Rms deviations from ideal values [52]			
Bond lengths (Å)	0.01	0.01	0.01
Bond angles (deg)	1.2	1.2	1.2
Average B -factor (Å ²)			
Protein	213	156	134
Ligand	201	132	175
MolProbity validation [48]			
Clashscore	13.48	10.12	13.46
MolProbity score (percentile) ^b	3.26 (81 st)	3.01 (88 th)	3.12 (83 rd)
Ramachandran plot			
Favoured (%)	86.5	90.7	90.4
Allowed (%)	10.9	7.2	7.6
Disallowed (%)	2.6	2.1	2.0
Protein Data Bank deposition			
PDB code	6NDP	6NDO	5UYR

^aValues for the outer shell are given in parentheses: D199A, 3.69–3.45 Å; L193Q, 4.00–3.89 Å; L193N, 3.80–3.58 Å.

^b100th percentile indicates the top structures of comparable resolution; 0th percentile indicates the bottom ones.

Crystallization, X-ray diffraction data collection and processing

Crystals of the L193Q, L193N and D199A variants in the presence of BV were grown from solutions containing

7–12% (w/v) PEG 4000, 0.2 M sodium acetate, 0.1 M Tris, pH 7.9–8.3, in a hanging drop vapour diffusion configuration as described previously [29]. Setting up of the drops was performed under green light, and crystallization trays

were kept in the dark covered in aluminium foil. Crystals were cryoprotected by a quick soak in crystallization solution added with 25% (w/v) PEG 400 and flash cooled in liquid nitrogen using Hampton Research loops (Aliso Viejo, CA, USA). For the visualization of the drops and manipulation of the crystal samples for cryo-cooling, minimal exposure to microscope light was applied using a green filter (passband: 450–600 nm, low-pass cut-off: 770 nm) (LEE Filters, Hampshire, UK).

X-ray diffraction data sets were collected at 100 K at the PROXIMA-1 and PROXIMA-2A protein crystallography beamlines at Synchrotron SOLEIL (L'Orme des Merisiers Saint-Aubin, Gif-sur-Yvette, France). Data were processed using XDS [41] and scaled using AIMLESS [42] from the CCP4 program suite [43], isolating 5% of the measured reflections for cross-validation purposes. Analysis of the Matthews coefficient [44] suggested the presence of two chains in the asymmetric unit. Detailed parameters and statistics of these steps are present in Table 3.

Structure determination, model building and refinement

The three crystal structures were solved by molecular replacement with Phaser [45] using the coordinates of wild-type *XccBphP* as a search model (PDB code: 5AKP) [24]. Restrained refinement and manual model building were then performed with the programmes Buster [46] and COOT [47], respectively. Due to the low resolution of the data, the initial refinements were done under LSSR restraints using the atomic coordinates from the 5AKP structure. The *B*-factors were refined as groups, and the BV molecules were introduced based on the coordinates of the wild-type protein.

Validation, analysis and graphical representation of the model

The final models were validated with MolProbity [48] as well as with the validation module implemented in COOT. Table S2 summarizes the statistics generated at these steps. The protein structure comparison service PDBeFold [49] at the European Bioinformatics Institute (<http://www.ebi.ac.uk/msd-srv/ssm>) was used for r.m.s.d. calculations. Molecular structures and their electron densities were represented using PYMOL version 1.8 (Schrödinger, New York, NY, USA).

Plant material and growth conditions

Arabidopsis thaliana (L.) Heynh. ecotype Col-0 seeds were used for stomatal aperture assays. Seeds were surface sterilized with an 96% ethanol, 50% bleach and water mixture (8 : 1 : 1) for 5 min and rinsed three times with ethanol.

Sterilized seeds were kept in the dark for 3 days at 4 °C. Plants were grown in Petri dishes containing half-strength Murashige and Skoog (MS) medium with 1% sucrose and 0.5 g·L⁻¹ MES hydrate under a 12 h : 12 h light/dark cycle (photon flux density of 90 μE) at 22–23 °C. The relative humidity was maintained between 60–70%. After a week, plants were transferred to a mixture of vermiculite, peat moss and perlite (1 : 1 : 1).

Stomatal bioassay

Stomatal bioassays were performed as previously described [28]. Epidermal peels from Col-0 leaves of 4-week-old plants were floated on a 10 : 10 buffer under light (10 mM KCl, 10 mM MES-KOH, pH 6.15) for 2.5 h. Then, bacterial suspensions at 10⁸ CFU·mL⁻¹ in the same buffer for each strain (previously grown in the dark) or 10 : 10 buffer (control) were added to the medium and incubated for another 1 h. Apertures from four independent experiments and 40 stomata per experiment were measured in a Carl Zeiss microscope (Oberkochen, Germany) (400×) with the aid of an eyepiece micrometre.

Xanthan production

Xanthan quantification in liquid culture was performed as previously described [12]. Briefly, bacterial strains were cultured in the dark or under red or far-red illumination for 48 h at 28 °C in 15 mL PYM liquid medium with the addition of 2% glucose in 50-mL flasks, using an orbital shaker rotating at 130 r.p.m. Then, after recording their OD₆₀₀ values, cultures were centrifuged (25 000 *g* for 40 min) and KCl was added to a final concentration of 1% to the supernatants. The crude xanthan was precipitated by adding 30 mL of 96% ethanol. All crude xanthan extracts and their corresponding cell pellets were collected, dried and weighed. Results are expressed as mg of xanthan per mg of cell pellet.

Acknowledgements

This work was supported by the Argentinian Research Council (CONICET), the Argentinian Agency for Science and Technology Promotion (ANPCyT) with grants awarded to HRB (PICT-2016-1425), VPC (PICT-2016-2872) and FM (PICT-2014-0710, PICT-2016-0232), and the Argentinian Ministry of Science, Technology and Productive Innovation (MINCyT). VPC and LT were supported by a postdoctoral scholarship from CONICET. LHO, JR, SK, FAG, AAV, FM and HRB are career researchers from CONICET. We are grateful for access to the PROXIMA-1 and PROXIMA-2A beamlines at Synchrotron SOLEIL, France (proposal number 20150716).

Conflict of interest

The authors declare no conflict of interest.

Peer Review

The peer review history for this article is available at <https://publons.com/publon/10.1111/febs.15883>.

Data accessibility

The atomic coordinates and structure factors have been deposited in the Protein Data Bank (<https://www.rcsb.org/>) under the accession codes **6NDP** (L193Q variant), **6NDO** (L193N variant) and **5UYR** (D199A variant). All data needed to evaluate the conclusions in this work are present in the paper. Additional data related to this paper are available upon request to the authors.

Author contributions

FM and HRB conceived and designed the experiments. VC, LT, SS, GTA, JR, SF, SK, FM and HRB performed the experiments. VC, LHO, LT, SS, JR, FM and HRB analysed the data. AAV, LMGC and FAG provided facilities. FM and HRB supervised the study. LHO, AAV, FAG, LMGC and HRB financed the project. VC, LHO, FM and HRB wrote and illustrated the paper.

References

- Auldridge ME & Forest KT (2011) Bacterial phytochromes: more than meets the light. *Crit Rev Biochem Mol Biol* **46**, 67–88.
- Mroginski MA, Murgida DH, von Stetten D, Kneip C, Mark F & Hildebrandt P (2004) Determination of the chromophore structures in the photoinduced reaction cycle of phytochrome. *J Am Chem Soc* **126**, 16734–16735.
- Rockwell NC, Su Y-S & Lagarias JC (2006) Phytochrome structure and signaling mechanisms. *Annu Rev Plant Biol* **57**, 837–858.
- Rottwinkel G, Oberpichler I & Lamparter T (2010) Bathy phytochromes in rhizobial soil bacteria. *J Bacteriol* **192**, 5124–5133.
- Velazquez Escobar F, Piwowarski P, Salewski J, Michael N, Fernandez Lopez M, Rupp A, Qureshi BM, Scheerer P, Bartl F, Frankenberg-Dinkel N *et al.* (2015) A protonation-coupled feedback mechanism controls the signalling process in bathy phytochromes. *Nat Chem* **7**, 423–430.
- Briggs WR & Olney MA (2001) Photoreceptors in plant photomorphogenesis to date. Five phytochromes, two cryptochromes, one phototropin, and one superchrome. *Plant Physiol* **125**, 85–88.
- Berry JO, Yerramsetty P, Zielinski AM & Mure CM (2013) Photosynthetic gene expression in higher plants. *Photosynth Res* **117**, 91–120.
- Ballaré CL & Pierik R (2017) The shade-avoidance syndrome: multiple signals and ecological consequences. *Plant Cell Environ* **40**, 2530–2543.
- Kumar S, Kateriya S, Singh VS, Tanwar M, Agarwal S, Singh H, Khurana JP, Amla DV & Tripathi AK (2012) Bacteriophytochrome controls carotenoid-independent response to photodynamic stress in a non-photosynthetic rhizobacterium, *Azospirillum brasilense* Sp7. *Sci Rep* **2**, 872.
- Wu L, McGrane RS & Beattie GA (2013) Light regulation of swarming motility in *Pseudomonas syringae* integrates signaling pathways mediated by a bacteriophytochrome and a LOV protein. *mBio* **4**, e00334-13.
- Ricci A, Dramis L, Shah R, Gärtner W & Losi A (2015) Visualizing the relevance of bacterial blue- and red-light receptors during plant-pathogen interaction. *Environ Microbiol Rep* **7**, 795–802.
- Bonomi HR, Toum L, Sycz G, Sieira R, Toscani AM, Gudesblat GE, Leskow FC, Goldbaum FA, Vojnov AA & Malamud F (2016) *Xanthomonas campestris* attenuates virulence by sensing light through a bacteriophytochrome photoreceptor. *EMBO Rep* **17**, 1565–1577.
- McGrane R & Beattie GA (2017) *Pseudomonas syringae* pv. *syringae* B728a regulates multiple stages of plant colonization via the bacteriophytochrome BphP1. *mBio* **8**, e01178-17.
- Woitowich NC, Halavaty AS, Waltz P, Kupitz C, Valera J, Tracy G, Gallagher KD, Claesson E, Nakane T, Pandey S *et al.* (2018) Structural basis for light control of cell development revealed by crystal structures of a myxobacterial phytochrome. *IUCrJ* **5**, 619–634.
- Mukherjee S, Jemielita M, Stergioula V, Tikhonov M & Bassler BL (2019) Photosensing and quorum sensing are integrated to control *Pseudomonas aeruginosa* collective behaviors. *PLoS Biol* **17**, e3000579.
- Moyano L, Carrau A, Petrocelli S, Kraiselburd I, Gärtner W & Orellano EG (2020) Bacteriophytochromes from *Pseudomonas syringae* pv. *tomato* DC3000 modulate the early stages of plant colonization during bacterial speck disease. *Eur J Plant Pathol* **156**, 695–712.
- Verma RK, Biswas A, Kakkar A, Lomada SK, Pradhan BB & Chatterjee S (2020) A bacteriophytochrome mediates interplay between light sensing and the second messenger cyclic Di-GMP to control social behavior and virulence. *Cell Rep* **32**, 108202.

- 18 Gourinchas G, Ettl S & Winkler A (2019) Bacteriophytochromes - from informative model systems of phytochrome function to powerful tools in cell biology. *Curr Opin Struct Biol* **57**, 72–83.
- 19 Ulijasz AT & Vierstra RD (2011) Phytochrome structure and photochemistry: recent advances toward a complete molecular picture. *Curr Opin Plant Biol* **14**, 498–506.
- 20 Burgie ES & Vierstra RD (2014) Phytochromes: an atomic perspective on photoactivation and signaling. *Plant Cell* **26**, 4568–4583.
- 21 Takala H, Björling A, Berntsson O, Lehtivuori H, Niebling S, Hoernke M, Kosheleva I, Henning R, Menzel A, Ihalainen JA *et al.* (2014) Signal amplification and transduction in phytochrome photosensors. *Nature* **509**, 245–248.
- 22 Yang X, Stojković EA, Ozarowski WB, Kuk J, Davydova E & Moffat K (2015) Light signaling mechanism of two tandem bacteriophytochromes. *Structure* **23**, 1179–1189.
- 23 Björling A, Berntsson O, Lehtivuori H, Takala H, Hughes AJ, Panman M, Hoernke M, Niebling S, Henry L, Henning R *et al.* (2016) Structural photoactivation of a full-length bacterial phytochrome. *Sci Adv* **2**, e1600920.
- 24 Otero LH, Klinke S, Rinaldi J, Velázquez-Escobar F, Mroginski MA, Fernández López M, Malamud F, Vojnov AA, Hildebrandt P, Goldbaum FA *et al.* (2016) Structure of the full-length bacteriophytochrome from the plant pathogen *Xanthomonas campestris* provides clues to its long-range signaling mechanism. *J Mol Biol* **428**, 3702–3720.
- 25 Gourinchas G, Vide U & Winkler A (2019) Influence of the N-terminal segment and the PHY-tongue element on light-regulation in bacteriophytochromes. *J Biol Chem* **294**, 4498–4510.
- 26 Vicente JG & Holub EB (2013) *Xanthomonas campestris* pv. *campestris* (cause of black rot of crucifers) in the genomic era is still a worldwide threat to brassica crops. *Mol Plant Pathol* **14**, 2–18.
- 27 An S-Q, Potnis N, Dow M, Vorhölter F-J, He Y-Q, Becker A, Teper D, Li Y, Wang N, Bleris L *et al.* (2020) Mechanistic insights into host adaptation, virulence and epidemiology of the phytopathogen *Xanthomonas*. *FEMS Microbiol Rev* **44**, 1–32.
- 28 Gudesblat GE, Torres PS & Vojnov AA (2009) *Xanthomonas campestris* overcomes *Arabidopsis* stomatal innate immunity through a DSF cell-to-cell signal-regulated virulence factor. *Plant Physiol* **149**, 1017–1027.
- 29 Klinke S, Otero LH, Rinaldi J, Sosa S, Guimarães BG, Shepard WE, Goldbaum FA & Bonomi HR (2014) Crystallization and preliminary X-ray characterization of the full-length bacteriophytochrome from the plant pathogen *Xanthomonas campestris* pv. *campestris*. *Acta Crystallogr Sect F Struct Biol Cryst Commun* **70**, 1636–1639.
- 30 Yang X, Kuk J & Moffat K (2008) Crystal structure of *Pseudomonas aeruginosa* bacteriophytochrome: photoconversion and signal transduction. *Proc Natl Acad Sci USA* **105**, 14715–14720.
- 31 Yang X, Kuk J & Moffat K (2009) Conformational differences between the Pfr and Pr states in *Pseudomonas aeruginosa* bacteriophytochrome. *Proc Natl Acad Sci USA* **106**, 15639–15644.
- 32 Antelo GT, Sánchez-Lamas M, Goldbaum FA, Otero LH, Bonomi HR & Rinaldi J (2020) A spectroscopy-based methodology for rapid screening and characterization of phytochrome photochemistry in search of Pfr-favoured variants. *Photochem Photobiol* **96**, 1221–1232.
- 33 Wagner JR, Zhang J, von Stetten D, Günther M, Murgida DH, Mroginski MA, Walker JM, Forest KT, Hildebrandt P & Vierstra RD (2008) Mutational analysis of *Deinococcus radiodurans* bacteriophytochrome reveals key amino acids necessary for the photochromicity and proton exchange cycle of phytochromes. *J Biol Chem* **283**, 12212–12226.
- 34 Takala H, Edlund P, Ihalainen JA & Westenhoff S (2020) Tips and turns of bacteriophytochrome photoactivation. *Photochem Photobiol Sci* **19**, 1488–1510.
- 35 Burgie ES, Wang T, Bussell AN, Walker JM, Li H & Vierstra RD (2014) Crystallographic and electron microscopic analyses of a bacterial phytochrome reveal local and global rearrangements during photoconversion. *J Biol Chem* **289**, 24573–24587.
- 36 Wagner JR, Zhang J, Brunzelle JS, Vierstra RD & Forest KT (2007) High resolution structure of *Deinococcus* bacteriophytochrome yields new insights into phytochrome architecture and evolution. *J Biol Chem* **282**, 12298–12309.
- 37 Beattie GA, Hatfield BM, Dong H & McGrane RS (2018) Seeing the light: the roles of red- and blue-light sensing in plant microbes. *Annu Rev Phytopathol* **56**, 41–66.
- 38 Dow JM, Fouhy Y, Lucey JF & Ryan RP (2006) The HD-GYP domain, cyclic di-GMP signaling, and bacterial virulence to plants. *Mol Plant Microbe Interact* **19**, 1378–1384.
- 39 Cadmus MC, Rogovin SP, Burton KA, Pittsley JE, Knutson CA & Jeanes A (1976) Colonial variation in *Xanthomonas campestris* NRRL B-1459 and characterization of the polysaccharide from a variant strain. *Can J Microbiol* **22**, 942–948.
- 40 Assafa TE, Anders K, Linne U, Essen L-O & Bordignon E (2018) Light-driven domain mechanics of a minimal phytochrome photosensory module studied by EPR. *Structure* **26**, 1534–1545.e4.

- 41 Kabsch W (2010) XDS. *Acta Crystallogr D Biol Crystallogr* **66**, 125–132.
- 42 Evans PR & Murshudov GN (2013) How good are my data and what is the resolution? *Acta Crystallogr D Biol Crystallogr* **69**, 1204–1214.
- 43 Winn MD, Ballard CC, Cowtan KD, Dodson EJ, Emsley P, Evans PR, Keegan RM, Krissinel EB, Leslie AGW, McCoy A *et al.* (2011) Overview of the CCP4 suite and current developments. *Acta Crystallogr D Biol Crystallogr* **67**, 235–242.
- 44 Kantardjieff KA & Rupp B (2003) Matthews coefficient probabilities: Improved estimates for unit cell contents of proteins, DNA, and protein-nucleic acid complex crystals. *Protein Sci* **12**, 1865–1871.
- 45 McCoy AJ, Grosse-Kunstleve RW, Adams PD, Winn MD, Storoni LC & Read RJ (2007) Phaser crystallographic software. *J Appl Crystallogr* **40**, 658–674.
- 46 Bricogne G, Blanc E, Brandl M, Flensburg C, Keller P, Paciorek W, Roversi P, Sharff A, Smart OS, Vornrhein C *et al.* (2011) BUSTER version XYZ. Global Phasing Ltd., Cambridge.
- 47 Emsley P, Lohkamp B, Scott WG & Cowtan K (2010) Features and development of Coot. *Acta Crystallogr D Biol Crystallogr* **66**, 486–501.
- 48 Chen VB, Arendall WB 3rd, Headd JJ, Keedy DA, Immormino RM, Kapral GJ, Murray LW, Richardson JS & Richardson DC (2010) MolProbity: all-atom structure validation for macromolecular crystallography. *Acta Crystallogr D Biol Crystallogr* **66**, 12–21.
- 49 Krissinel E & Henrick K (2004) Secondary-structure matching (SSM), a new tool for fast protein structure alignment in three dimensions. *Acta Crystallogr D Biol Crystallogr* **60**, 2256–2268.
- 50 Afonine PV, Moriarty NW, Mustyakimov M, Sobolev OV, Terwilliger TC, Turk D, Urzhumtsev A & Adams PD (2015) FEM: feature-enhanced map. *Acta Crystallogr D Biol Crystallogr* **71**, 646–666.
- 51 Liebschner D, Afonine PV, Baker ML, Bunkóczi G, Chen VB, Croll TI, Hintze B, Hung LW, Jain S, McCoy AJ *et al.* (2019) Macromolecular structure determination using X-rays, neutrons and electrons: recent developments in Phenix. *Acta Crystallogr D Struct Biol* **75**, 861–877.
- 52 Engh RA & Huber R (1991) Accurate bond and angle parameters for X-ray protein structure refinement. *Acta Crystallogr A* **47**, 392–400.

Supporting information

Additional supporting information may be found online in the Supporting Information section at the end of the article.

Supplementary material.